Purdue University
Purdue e-Pubs

Birck and NCN Publications | Birck Nanotechnology Center

12-2009

# Identification of multiple oscillation states of carbon nanotube tipped cantilevers interacting with surfaces in dynamic atomic force microscopy

Mark Strus
*Purdue University - Main Campus*, mstrus@gmail.com

Arvind Raman
*Purdue University - Main Campus*, raman@purdue.edu

Follow this and additional works at: http://docs.lib.purdue.edu/nanopub

Part of the Nanoscience and Nanotechnology Commons

Strus, Mark and Raman, Arvind, "Identification of multiple oscillation states of carbon nanotube tipped cantilevers interacting with surfaces in dynamic atomic force microscopy" (2009). *Birck and NCN Publications.* Paper 473.
http://docs.lib.purdue.edu/nanopub/473

This document has been made available through Purdue e-Pubs, a service of the Purdue University Libraries. Please contact epubs@purdue.edu for additional information.

# Identification of multiple oscillation states of carbon nanotube tipped cantilevers interacting with surfaces in dynamic atomic force microscopy

Mark C. Strus and Arvind Raman*

*Birck Nanotechnology Center and School of Mechanical Engineering, Purdue University, West Lafayette, Indiana, 47907 USA*

(Received 19 May 2009; revised manuscript received 14 September 2009; published 17 December 2009)

Carbon nanotubes (CNTs) have gained increased interest in dynamic atomic force microscopy (dAFM) as sharp, flexible, conducting, nonreactive tips for high-resolution imaging, oxidation lithography, and electrostatic force microscopy. By means of theory and experiments we lay out a map of several distinct tapping mode AFM oscillation states for CNT tipped AFM cantilevers: namely, noncontact attractive regime oscillation, intermittent contact with CNT slipping or pinning, or permanent contact with the CNT in point or line contact with the surface while the cantilever oscillates with large amplitude. Each state represents fundamentally different origins of CNT-surface interactions, CNT tip-substrate dissipation, and phase contrast and has major implications for the use of these probes for imaging, compositional contrast, and lithography. In particular, we present a method that uses energy-dissipation spectroscopy to identify if the CNT slips laterally on the surface or remains pinned in the intermittent contact regime. By comparing phase contrast images and energy dissipation on graphite, graphene oxide, and silicon oxide surfaces, we demonstrate the utility of the method in identifying pinning or slipping of the CNT on the surface in the intermittent contact regime.

DOI: 10.1103/PhysRevB.80.224105 PACS number(s): 62.25.−g, 34.35.+a, 07.79.Lh, 81.07.De

## I. INTRODUCTION

Since their inception,[1] carbon nanotubes have been developed as ideal tips for atomic force microscopy (AFM) because their low reactivity[2] and hydrophobicity[3] minimize surface contamination, their small diameters lead to improved lateral resolution,[4–7] and their high-aspect ratios eliminate concerns of tip wear.[8] The unique electrical and mechanical properties of single-walled (SW) and multiwalled (MW) CNT AFM probes have been used to improve tunneling,[9,10] magnetic,[11,12] current-sensing,[13,14] and surface potential[15,16] scanning-probe microscopy as well as scanning nanolithography.[17–19] CNTs can reversibly bend under large loads preventing damage to imaged biomolecules,[20,21] and novel functionalization of CNTs can be used for biochemical sensing[22–25] and imaging under liquids.[26–28]

In general, CNT AFM probes are harmonically excited near resonance and used to image substrates when dynamically operated in either an attractive[29] or repulsive regime[30] using tapping-mode or amplitude-modulated (AM) AFM. When CNT AFM probes are operated in the net repulsive regime, also known as intermittent contact, CNTs have the potential to buckle, bend, kink, adhere, and slide. For example, Lee *et al.*[31] showed how the excitation of the microcantilever's higher harmonics could be used to identify CNT buckling during intermittent contact and demonstrated how buckling could lead to image artifacts. Solares *et al.*[30] compared molecular-dynamics (MD) interaction models with experiments to explain how SWCNT AFM probes could experience multistable solutions during intermittent contact, especially if sample adhesion and friction were significant. The freely sliding, MD model of SWCNT tips and experimental validation of Kutana *et al.*[32] suggested that CNT kinking could lead to sudden force drops and increasing vibration amplitudes, particularly during permanent contact. Each of these studies highlight the fact that the CNT mechanics, particularly the tip-sample boundary condition, play an important role in the CNT AFM stability.

Through several frequency-modulated AFM studies of CNT AFM probes, Marsaudon *et al.*[33–36] were able to identify three imaging regimes, noncontact, intermittent, and permanent contact, through experimental frequency-shift approach curves and a simple CNT-interaction model that accounted for the CNT stiffness and adhesion pull-off force. Because these results assume energy dissipation from friction is generally small compared to adhesion hysteresis, CNT pinning or slipping is not emphasized nor are surfaces with different roughnesses and adhesion thoroughly investigated. Instead, the CNT boundary condition is estimated by using the frequency shift to empirically calculate the CNT stiffness. Finally, it is not clear which of these observed states would be encountered in the commonly used tapping mode or AM-AFM, which is presently the most widely used dynamic AFM mode.

The current work investigates multiple imaging regimes of CNT probes in tapping mode or AM-AFM, specifically demonstrating, in addition to the noncontact oscillation regime, the existence of multiple oscillating states: (a) two types of permanent contact, where the cantilever continues to oscillate with significant amplitude while the CNT tip is permanently anchored to the substrate either touching it at its tip (point contact) or adhered to it along some of its length (line contact) and (b) two kinds of intermittent contact, where the cantilever oscillates in a manner that the CNT tip intermittently taps on the substrate, with the CNT either slipping or pinned during the intermittent contact. These oscillation states have important implications for lithography, compositional mapping, and biological sensing of samples using such probes. The identification of the permanent point and line contact is made by comparing the experimental average force-distance curves as the oscillating probe is brought closer to the surface with experimental static-force-distance curves and with theory. The identification of CNT pinning and slipping during intermittent contact is based on phase and energy-dissipation spectroscopy. We discuss the implica-

 ©2009 The American Physical Society

TABLE I. Table of CNT and CNT-substrate interaction properties input into the perfect slip and pin model in Fig. 3. The values for $\theta_o$, $d_i$, $d_o$, and $L$ are based on CNT1 in Fig. 2(a). The CNT bending modulus, $E$, chosen to mimic static-force-distance experiments, is slightly larger than observed experimentally for CVD-grown MWCNTs (Ref. 48). The CNT-substrate interaction parameters, $\Phi_o$, $\rho$, and $R_o$, are scaled up from SWCNT studies (Ref. 47), where interaction forces are assumed to act only between the outermost nanotube shell and the substrate, though all the shells contribute to the bending stiffness of the nanotube (Ref. 39).

| $E$ (TPa) | $d_i$ (nm) | $d_o$ (nm) | $L$ ($\mu$m) | $\theta_o$ (deg) | $\Phi_o$ (J/m) | $\rho$ (nm) | $R_o$ (nm) | $K$ (N/m) |
|---|---|---|---|---|---|---|---|---|
| 0.6 | 10 | 41 | 2.1 | 81 | 1.37 | 1.36 | 1.68 | 19000 |

tions of CNT pinning and slipping, both as obstacle for accurate topography measurements or CNT tip based oxidation lithography and as a potential method of analyzing surface composition.

## II. THEORETICAL ANALYSIS OF STATIC-FORCE-DISTANCE CURVES

Because it is difficult to directly observe the behavior of CNT AFM probes operated in dAFM, it is useful to first understand, theoretically, the mechanics of CNTs on samples with different friction properties through static force versus distance curves. The underlying adhesive nanomechanics of CNT-surface interactions was studied with an inextensible elastica model[37] of a MWCNT, interacting with a graphite surface through van der Waals forces,[38] the details of which can be found in Ref. 39. Though localized kinking[32] is not included, continuum elastica models have proven useful for modeling high-aspect ratio CNTs[40] and nanowires,[41] which are known to endure elastic deformations elastically.[42] The particular model used here has been previously used to study the adhesive nanomechanics of MWCNTs peeled from various inorganic and polymer surfaces,[39,43] and has been subsequently validated with molecular dynamics[44] and direct scanning electron microscopy observations.[45] The fundamental difference in the current work is that the CNT is now brought nearly perpendicular to the surface.

The model of an inextensible highly flexible rod interacting with a graphite substrate can be defined as a boundary-value problem consisting of three ordinary differential equations[46] representing the balance of moments and the balance of forces in the $z$ and $x$ directions

$$EI\frac{d^2\theta}{ds^2}(s) = -\gamma(s)\cos\theta(s) - \varphi(s)\sin\theta(s),$$

$$\frac{d\gamma}{ds}(s) = f(s), \quad \frac{d\varphi}{ds}(s) = 0, \tag{1}$$

where $s$ is the arc length coordinate along the CNT, such that $s=0$ at the CNT free end to $s=L$ at the end where the CNT is attached to the cantilever tip[39] while $\theta(s)$ is the angle the CNT makes with the horizontal at each point along the CNT. The vertical and horizontal force per unit length along the tube are, respectively, shown as $\gamma(s)$ and $\varphi(s)$ while $f(s)$ represents the CNT-substrate interaction force from van der Waals interactions. The quantities $E$, $L$, $d_o$, $d_i$, and $I = \pi/64(d_o^4 - d_i^4)$ refer to the respective flexural elastic modulus, length, inner diameter, outer diameter, and area moment of inertia of the CNT. In addition to these equations, inextensibility criteria and geometric constraints must be included such that

$$\frac{dz}{ds}(s) = \sin\theta(s), \quad \frac{dx}{ds}(s) = \cos\theta(s), \quad P = \int_0^L f(s)ds, \tag{2}$$

which states that the external (static) force, $P$, applied to the CNT, through the microcantilever tip as its pushed toward the surface, must equal the cumulative sum of CNT-substrate interaction forces. The interaction force per unit length between the CNT and substrate is defined as[38,47]

$$f(s) = 6.119\frac{\Phi_o}{R_o - \rho}\left(\left[\frac{1}{1 + \frac{0.09179}{R_o - \rho}z(s)}\right]^5 - \left[\frac{1}{1 + \frac{0.09179}{R_o - \rho}z(s)}\right]^{11}\right), \tag{3}$$

where $\Phi_o$ is the depth of the potential energy well per unit length between the CNT and substrate, which depends solely on the radius, $R_o$, of the outermost CNT shell, and $\rho$ is the equilibrium separation between the graphite substrate and the center of the CNT. This CNT-graphite surface interaction, derived by Coffin *et al.*[47] to predict decohesion of CNT bundles, is based on the universal graphitic potential of Girifalco *et al.*[38] which demonstrated that the interaction potential between various carbon molecules could be simplified into a simply analytic form. Table I shows all of the input quantities for the model, which have been primarily based on CNT1 in Fig. 2(a). While the model is developed for carbon nanotubes interacting with graphitic surfaces, it also qualitatively captures carbon nanotube interactions with other surfaces.[43]

With AUTO, a software capable of numerically continuing the solutions of boundary-value problems,[50] Eqs. (1) can be solved once appropriate boundary conditions are defined

$$\frac{d\theta}{ds}(0) = 0, \quad \theta(L) = \theta_o, \quad \varphi(0) = Kx(0). \tag{4}$$

Respectively, the boundary conditions account for no moments at the free end, the angle from normal the CNT makes

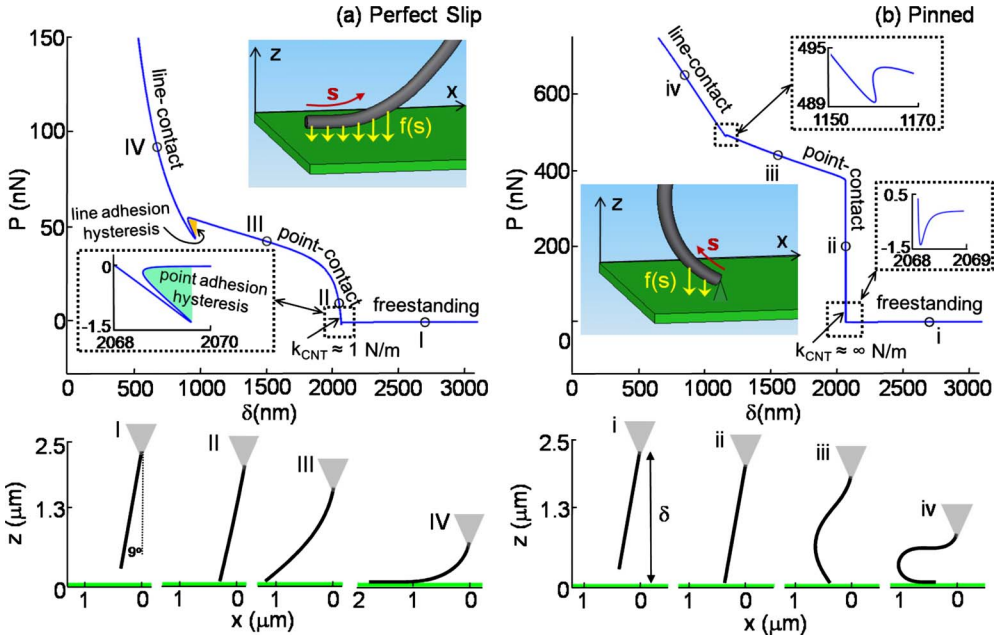


FIG. 1. (Color online) Large deformation continuum elastica (Ref. 37) model of the static forces required to push a MWCNT toward a graphite surface as a function of the $\delta$, the distance between the substrate and CNT-microcantilever attachment point. The boundary-value problem (Ref. 39) was numerically solved using AUTO (Ref. 50) for both (a) perfect slip and (b) pinned boundary condition at the CNT tip graphite interface. The van der Waals interaction forces between the CNT and graphite surface, $f(s)$, are modeled through a universal graphitic potential (Refs. 38 and 47) while the MWCNT parameters are taken from CNT1 in Fig. 2 as shown in Table I. The numerically solved CNT shapes for the perfect slipping (I–IV) and perfect pinning (i–iv) cases demonstrated how the CNT transitions between possible configurations.

from horizontal ($\theta$=81° from CNT1), and a slipping or pinning condition which can be adjusted by setting the horizontal spring constant ($K$) to either null (slip) or a large value (pin).

Two ideal cases are studied using the theoretical model, both representing extremes of possible boundary conditions on the CNT: (a) free sliding where the only interaction forces are normal to the surface while frictional forces are negligible and (b) when the CNT tip is not allowed to slide laterally on the surface (i.e., pinned) by means of a stiff horizontal spring that penalizes such motion. Figure 1 shows the static forces required to push a MWCNT against a flat graphite substrate as function of $\delta$ for the parameter values described in Table I, the distance between the surface and the CNT-microcantilever attachment point ($s=L$). Although relative $z$-piezo distances, $z_r$, are measured at the microcantilever base rather than tip, microcantilever deflections are negligible compared to the micrometer base movement, such that $\delta$ is approximately equivalent to $z_r$ experimentally.[39]

In Fig. 1(a), lateral forces are neglected allowing the CNT to slip along the surface. As shown by the *theoretically predicted* CNT shapes (I–IV), the CNT starts far from the surface in a freestanding configuration (I) with an initial angle 9° from normal. When the CNT contacts the surface at a point, the static force increases (II) with a slope of $\approx 1$ N/m, then gradually plateaus (III) as the CNT bends and its tip slides along the surface. As the force plateaus, the slope of the $P$-$\delta$ curve stabilizes to a value slightly less than the theoretical bending stiffness of the CNT ($k_{CNT}=3EI/L^3$), as sliding become small and bending dominates. After significant bending, the CNT transitions from a *point-contact configuration* to a *line-contact configuration* (IV), where the CNT is adhered to the along its length and very large forces are required to further push the CNT toward the graphite surface. Whenever the CNT transitions from one configuration to the next, multiple stable solution branches can coexist for the same $\delta$. This coexistence is especially important near the freestanding to point-contact transition [see Fig. 1(a) inset], where the CNT may follow a different equilibrium solution when approaching or retracting,[43] leading to energy losses from *point-contact adhesion hysteresis*.[36] A similar *line-contact adhesion hysteresis* is expected whenever the CNT transitions from a line contact to point contact as indicated in Fig. 1(a).

In Fig. 1(b), a horizontal linear spring with large stiffness restricts the CNT from sliding at the CNT-substrate boundary and thus represents a pinned boundary condition for the CNT on the surface. In this example, the forces increase immediately with a near infinite slope when the freestanding CNT makes a point contact with the surface because the CNT is unable to slide. As the CNT is further pressed toward the surface (iii), the force increases linearly with distance as the CNT, still in point contact, begins to bend. Eventually, the CNT transitions into a line contact (iv). Although the CNT bends in both perfect slip and perfect pin models, when the CNT is pinned, the applied force is geometrically directed toward axial compression of the CNT rather than flexural bending, leading to the larger CNT stiffness. The pinned model is really an extreme case, as some CNT-substrate slipping is experimentally expected, even for samples with large friction coefficients.

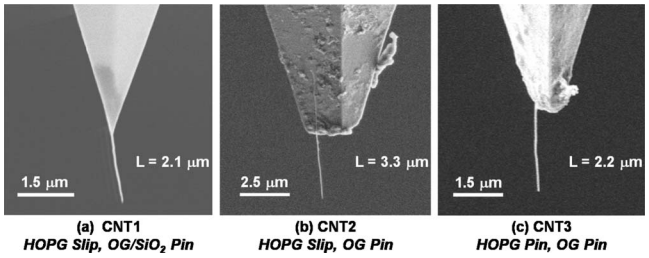


FIG. 2. Images of the three MWCNTs used to collect all of the presented experimental data. Each CNT has been labeled according to whether it slips or primarily pins on a given surface. The field-emission scanning-electron microscope was used to calculate the CNT lengths while labels indicate whether a CNT slipped or pinned on a specific surface. Based on Ref. 49, the spring constants of the microcantilevers for each CNT were (a) 3.5, (b) 24, and (c) 29 N/m, respectively. Transmission electron microscopy statistical analysis of the CNT source revealed typical inner and outer diameters $10 \pm 2$ and $40 \pm 6$ nm.

The theoretical models are thus important for visualizing the several configuration changes (freestanding, point contact, and line contact) that the CNT experiences when pushed into a surface as well as explaining the origin of adhesion hysteresis when a CNT approaches and then retracts from a surface. When the CNT-surface boundary condition is changed, the force-distance responses show dramatic differences including (a) much greater CNT stiffness in the pinned case compared to the perfect slip case and (b) maximum point-contact forces that are an order of magnitude larger when pinning than slipping. These theoretical characteristics will be used to identify CNT states in static and dAFM experiments.

## III. EXPERIMENTAL METHODS

Several chemical-vapor deposition (CVD) MWCNT AFM probes were fabricated according to the method described in Ref. 51 though the presented experimental results focus on the three probes in Fig. 2. The bending stiffness of each microcantilever was calibrated according to Ref. 49 while sensitivities were obtained from static-force-deflection curves where the conical AFM tip was pressed into a hard surface. In order to properly resolve the static CNT behavior, microcantilevers with soft stiffnesses ($<5$ N/m) were required. Three surfaces were tested, silicon oxide ($SiO_2$), highly ordered pyrolytic graphite (HOPG), and exfoliated oxidized graphene (OG) sheets which were prepared on HOPG samples according to Ref. 52. All of the experiments were performed with Agilent 5500™ AFM system and most were obtained in a dry nitrogen chamber with $\approx 0\%$ relative humidity, though independent humidity studies up to ambient conditions of 35% showed no significant influence on the results.

## IV. EXPERIMENTAL ANALYSIS OF STATIC-FORCE-DISTANCE CURVES

Though several groups have measured static-force distance with CNTs and demonstrated nonlinear forces due to CNT bending, kinking, and sliding,[32,53–55] none have explicitly demonstrated if or when CNTs pin or slip on the surface nor identified all the different configurations of CNTs during this process. Figure 3 shows experimental static-force measurements for CNT1 on both HOPG and $SiO_2$.

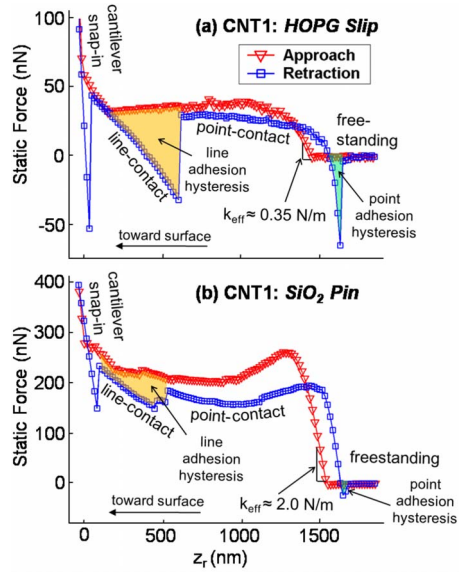


FIG. 3. (Color online) Static force-distance curve for CNT1 on (a) HOPG obeys the same general trends as the slipping model in Fig. 1(a) including a force plateauing effect during point contact, a linear force increase during line contact, and adhesion hysteresis during retraction. When approaching the surface, the microcantilever eventually snaps to the surface after the CNT line contact, as indicated by *cantilever snap in*. This slope was used to calibrate the probe sensitivity. When CNT1 was tested on (b) a $SiO_2$ substrate, a large initial static-force increase was observed, similar to the perfect pinning model in Fig. 1(b), while an abrupt slope change, similar to (a), is indicative of the transition from point to line contact.

On HOPG, static forces [see Fig. 3(a)] initially increase with a gentle slope of 0.35 N/m, which is estimated by linearly fitting the force-distance curve for the first 15 nm of CNT deformation after initial contact. When CNT1 is further pressed toward the sample, the experimental force increases suddenly and linearly with a slope=0.16 N/m around $z_r \approx 360$ nm. In the slipping model, when the CNT switches from point to line contact, a similar sudden slope change from 0.019 to 0.14 N/m occurs. As $z_r$ is further reduced in Fig. 3(a), the microcantilever snaps into the sample as indicated. By comparing the experimental force-distance changes in magnitude and slope to the theoretical slipping model in Fig. 1(a), the appropriate line-contact, point-contact, and freestanding CNT configurations can be labeled accordingly as in Fig. 3.

Also in Fig. 3(a), the retraction curve differs from approach curve whenever the CNT follows a different equilibrium branch, a trend predicted by the model and experimentally demonstrated with peeling of MWCNTs.[39,43] Sudden force jumps during retraction highlight the transition from line contact to point contact and from point contact to freestanding as the CNT suddenly switches from one equilibrium state to another. Note that the entire retraction curve appears

shifted to the right, especially during point contact, which has been ascribed to $z$-piezo hysteresis, an effect observed in previous CNT AFM probe studies with such large $z$-piezo ranges.[53,54]

In Fig. 3(b), static-force-distance measurements on $SiO_2$ with the same probe are quite different, as the force increases rapidly with an initial slope=2.0 N/m, up to a maximum value of 260 nN, a value nearly seven times larger than the maximum 40 nN point-contact force on HOPG. Note this difference in maximum point-contact forces was previously observed between the perfect slipping and pinning models. The differences between the experimental slopes for CNT1 on HOPG and $SiO_2$ can be explained by the change in the CNT stiffness. The static-force-distance slope is a measure of the probe's effective spring constant ($k_{eff}$), which is a combination of the microcantilever ($k_{cant}$) and CNT ($k_{\mathrm{CNT}}$) stiffnesses

$$\frac{1}{k_{eff}} = \frac{1}{k_{\mathrm{CNT}}} + \frac{1}{k_{cant}}, \tag{5}$$

where $k_{cant}$=3 N/m was empirically calculated using the method of Ref. 49. Using Eq. (5), the stiffness contribution of the CNT, $k_{\mathrm{CNT}}$, is calculated to be 0.68 N/m on HOPG and 6.0 N/m on $SiO_2$. The value of $k_{\mathrm{CNT}}$ depends on the CNT-substrate boundary condition[36] and whether the tip-sample forces primarily bend the CNT (slipping) or axially deform the CNT (pinning). The order of magnitude difference in $k_{\mathrm{CNT}}$ follows the trend from the theoretical model in Fig. 1 and highlights how the CNT-surface boundary (perfect slip or pinning or somewhere in between) critically affects the response of the CNT AFM probe in the point and line-contact regimes.

## V. IDENTIFICATION OF DIFFERENT OSCILLATION REGIMES

It is interesting to ask what happens when an *oscillating* probe with CNT tip is brought close to the sample surface. Figure 4 shows the dynamic amplitude- and average-force-approach curves for CNT1 on HOPG and $SiO_2$ at the cantilever's resonance frequency ($w_c$=98.6 kHz). The probe, initially excited with an unconstrained amplitude of 115 nm, experiences a reduction in amplitude in the region-labeled intermittent contact,[33] first from net attractive and then repulsive van der Waals forces[56] as the CNT taps intermittently on the surface [see details in Fig. 5(a)]. This distinction between attractive and net repulsive oscillations states is made in the usual way using phase response.[56]

As the microcantilever base is further lowered toward the surface, the oscillation is not large enough to overcome the CNT-substrate adhesion[36,57] and the CNT pulls into permanent contact with the surface ($z_r$<1500 nm). In this state, the CNT remains fixed to the substrate at its tip while the microcantilever continues to oscillate as the CNT either bends or slides on the surface. More specifically, a qualitative comparison of the static-force measurements in Fig. 3 and the average forces in Fig. 4 suggests that the CNT is in a *permanent point contact* until $z_r \approx 280$ nm where the average force increases linearly while the amplitude drops suddenly. Here, the CNT has switched from a permanent point contact to *permanent line contact*.

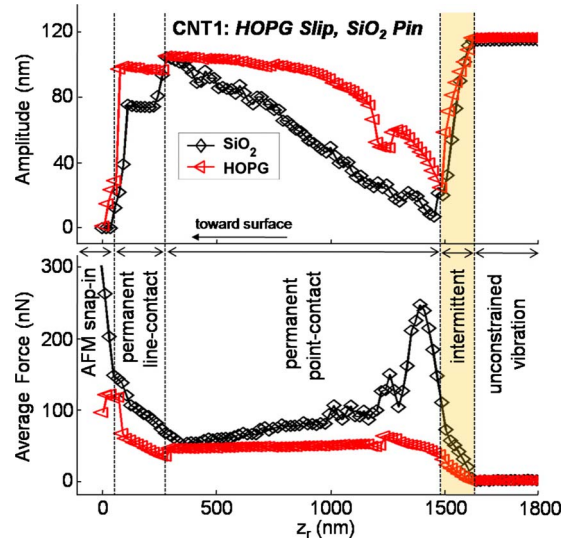


FIG. 4. (Color online) The dAFM oscillation states for CNT1 are shown via approach amplitude-distance curves on both HOPG and $SiO_2$. The CNT AFM probe vibrates at its unconstrained amplitude until brought close to the surface where van der Waals forces reduce the amplitude during intermittent contact. Average force-distance curves, qualitatively similar to previous static-force-distance curves, help identify permanent point contact, permanent line contact, and eventual snap in of the AFM microcantilever.

Often, during permanent point contact, the amplitude will increase with a reduction in $z_r$ (Refs. 6, 32, 57, and 58) as shown in Fig. 4. For SWCNTs, Kutana *et al.*[32] suggested this amplitude increase was an artifact of nonlinear kinking but with the demonstrated slipping behavior of the CNT, we suggest an alternate explanation. As soon as permanent point contact is initiated, the CNT acts as a repulsive spring between the cantilever and substrate, which leads to an increase in the resonant frequency of microcantilever (see Fig. 5 inset). Because the driving frequency, $\Omega$, is fixed in the tapping mode, the CNT AFM probe will thus be excited below resonance and therefore *at a lower amplitude*, as confirmed by a phase shift below 90° resonance (not shown). Because the CNT is able to slip more easily on HOPG, the increase in amplitude occurs much more quickly than it does on $SiO_2$, where lateral (frictional) forces are much larger (see Fig. 4).

The qualitative similarities between average force and static-force measurements are useful for identifying the (a) noncontact, (b) intermittent point contact, (c) permanent point contact, and (d) permanent line contact of the CNT on the surface. However, the important remaining question is: *"how do we identify if the CNT tip in the intermittent contact regime is actually pinned or slipping or somewhere in between?"* This knowledge is particularly important for critical dimension AFM (Ref. 59) and nanolithography,[18,19] where slipping could distort accurate topographical measurements or precise device fabrication. On the other hand phase imaging with slipping CNTs could enhance phase contrast depending on the substrate's frictional properties.

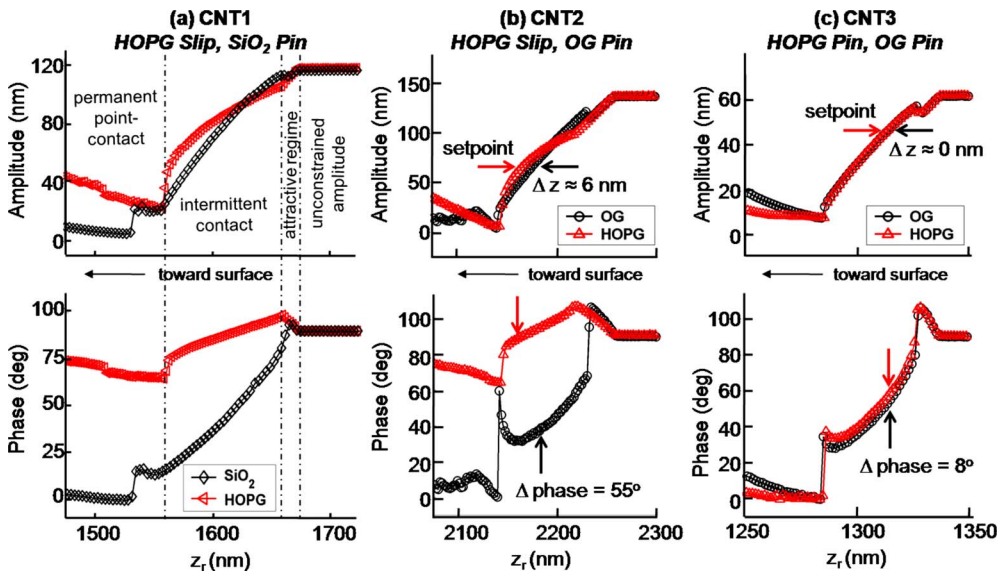


FIG. 5. (Color online) (a) Changes in the amplitude- and phase-distance approach curves are used to identify the oscillation states as CNT1 approaches HOPG and $SiO_2$ substrates. [(b)–(c)] The dAFM approach curves for CNT2 and CNT3 on HOPG and OG show how phase can be used to identify CNT slipping. The lack of phase difference, during intermittent contact, for CNT3 suggests this probe remains pinned in both cases. The red and black arrows in (b) and (c) indicate the amplitude set point and corresponding phase that was used to obtain the images Fig. 7. The differences in $z$ height on the two samples demonstrate the potential for topographical artifacts while the change in phase highlights the potential for enhanced phase contrast.

## VI. IDENTIFICATION OF CNT PINNING OR SLIPPING IN THE INTERMITTENT CONTACT REGIME USING POWER DISSIPATION SPECTROSCOPY

We now present a method using phase contrast and energy dissipation spectroscopy that is able to distinguish if the CNT slides laterally or remains mostly pinned during intermittent contact. In general, the length, angle orientation, and free-end geometry (capped, open, presence of dangling bonds, and leftover catalyst) of CNTs vary significantly from one AFM probe to the next, depending on the manufacturing process. Coupled with the fact that the roughness, coefficient of friction, and elasticity of tested samples are usually initially unknown to the user, CNT slipping or pinning is difficult to predict *a priori*. Here, we present a clear experimental signature for determining CNT pin or slip in the intermittent contact regime regardless of operating conditions or CNT imperfections.

Figure 5(a) shows the initial dAFM oscillation states when CNT1 approaches HOPG and $SiO_2$ surfaces. The initial amplitude reduction is caused by net attractive van der Waals forces as confirmed by the phase increase from 90°.[56] The transition to intermittent contact is characterized both by the change in-phase direction (from increasing to decreasing) and by the nonlinear decrease in amplitude.[31] An abrupt shift in phase and amplitude increase signal a transition from intermittent contact to permanent point contact.

Though similar characteristic transitions are observed for CNT2 and CNT3 on both HOPG and OG, [see Figs. 5(b) and 5(c)], the phase difference in the repulsive regime for CNT1 and CNT2 on HOPG and $SiO_2$/OG, respectively, is dramatic and particularly useful for distinguishing between CNT slipping and pinning. For example, the static-force response of CNT1 already indicated that CNT slides readily on HOPG and pins initially on $SiO_2$. In Fig. 5(a), when the probe is intermittently tapping, the phase lag is 20°–70° larger on HOPG than $SiO_2$. Similarly, intermittent contact phase lag for CNT2 is 40°–60° larger on HOPG than OG, a sample known to have larger lateral friction.[52] On the other hand, the phase-distance curves of CNT3 on HOPG and OG show very little phase difference and appear qualitatively similar to CNT2's response on OG, suggesting that CNT3 does not slip on either OG or HOPG.

This enhanced phase contrast is due in part by the different tip-sample dissipation mechanisms as the CNT slides or pins. In AM-AFM in the intermittent contact regime, the dissipation per cycle can be calculated directly from dynamic amplitude- and phase-distance curves using the formula from (Ref. 60),

$$P_c = \frac{1}{2}\frac{k_c\omega_c}{Q_c}\left[Q_c A_d A \sin(\phi) - A^2\frac{\omega_c}{\Omega}\right], \tag{6}$$

where $k_c$, $\omega_c$, and $Q_c$ are the respective stiffness, resonant frequency, and quality factor of the microcantilever, $A_d$ is the drive amplitude of the dither piezo, $\Omega$ is the driving frequency, and $A$ and $\phi$ are the measured amplitude and phase of microcantilever. Equation (6) allows for direct calculation of tip-sample dissipation from amplitude- and phase-distance curves, which can be used to highlight the slipping behavior of CNT AFM probes.

Based on data from Fig. 5, the dissipation *during intermittent contact* has been plotted in Figs. 6(a)–6(c) for all three probes as a function of $z$-piezo distance. Two different types of dissipation curves are present, depending on the probe and substrate. For CNT1, the tip-sample dissipation on

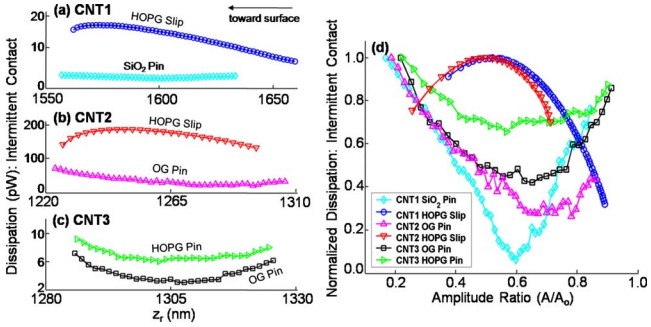


FIG. 6. (Color online) [(a)–(c)] Dissipation per oscillation cycle for the three CNT AFM probes in Fig. 2 on different samples. Only data in the intermittent contact regime are shown. In general, dissipation is larger on HOPG than either $SiO_2$ or OG for a given tip with similar parameters. Slipping dissipation is not only significantly larger but displays a concave down dependence as opposed to the constant dissipation during pinning. (d) When the dissipation curves are normalized to distinguish between the different dissipative mechanisms (Ref. 61), the presence of a different dissipation mechanism due to CNT slipping is clear from the concave up, amplitude-dependent shape for CNT1 and CNT2 on HOPG contrasted with the nearly flat dissipation when CNTs are pinning.

HOPG is an order of magnitude larger than SiO2 but more significantly the curve tends to follow a concave down shape as a function of CNT approach distance whereas dissipation on $SiO_2$ remains relatively constant. The dissipation for CNT2 is similar with HOPG showing a concave down shape and magnitude double that of the relatively flat signature on OG. On the other hand, the dissipation curves for CNT3 on HOPG and OG are extremely similar, both demonstrating a relatively constant value. Clearly there are two types of power dissipation profiles observed with these probes: either a concave down power dissipation versus $z_r$ or a relatively constant power dissipation versus $z_r$.

In general, tip-sample dissipation in the intermittent contact regime is expected to arise from (a) CNT-surface point-contact adhesion,[34] (b) CNT-surface lateral friction while sliding,[62] and (c) residual CNT vibrations following detachment from surface in each oscillation cycle. To further demonstrate that the underlying dissipative processes for CNT slipping and pinning are distinct in these two power dissipation profiles, it is useful to use the approach of Garcia *et al.*,[61] where dissipation on a sample is normalized by the maximum value and the amplitude is normalized with respect to the unconstrained vibration amplitude [Fig. 6(d)]. Clearly the normal power dissipation profiles fall into two distinct sets of curves. The first set of curves where the power dissipation is concave down with respect to the setpoint ratio $A/A_o$ occurs for CNT1 and CNT2 on HOPG, both where the CNT is expected to slip on the surface based on the static-force-distance curves. The dissipation tends to peak near an amplitude ratio of 0.5–0.6, where average tip-sample forces are known to be largest for conventional AFM probes.[63] Furthermore, the power dissipation profile for these cases is identical to that expected from sample friction or viscoelasticity[61] leading us to conclude that the primary source of dissipation in these cases (CNT1 and CNT2 on HOPG) is friction due to CNT slip.

On the other hand for all the other cases where the static-force-distance curves suggest CNT pinning on surface, the dissipation versus setpoint amplitude is relatively constant particularly in the middle of the graph suggestive of CNT-surface adhesion hysteresis.[36] However, the power dissipation profiles are curved up slightly indicating that perhaps other mechanisms such as CNT residual vibrations following detachment from sample may play a role.

The striking differences in power dissipation profiles between CNT pin and slip cases suggest the following experimental identification protocol: *a concave down trend in the normalized dissipation versus amplitude ratio with a peak near the center of total amplitude reduction can be used to identify CNT slipping on a surface, whereas relatively constant trends suggest lateral forces are large enough to pin the CNT so that the main source of dissipation is the hysteretic point-contact adhesion and CNT vibrations upon detachment from the surface.*

## VII. IMPLICATIONS OF CNT OSCILLATION STATES, SLIPPING, AND PINNING

The ability to identify permanent point contact and permanent line contact is of particular interest to CNT nanolithography,[64] where current conduction depends on good mechanical contact.[13] Typically, lithographic lines are made by physically scanning AFM probes[65] whereas the ability to directly place a CNT into a line contact could be useful for stably creating small diameter lines instantly. Line-contact imaging also has the potential to stimulate a new realm of biological sensing where CNTs, coated with key biological materials such as amino acids or DNA along their lengths, are selectively brought into different line contacts to control and manipulate the number of biochemical bindings. Line contacts have also been shown to be relevant for characterizing CNT-surface interfacial energies,[39] particularly for improving the fabrication and design of polymer nanocomposites.[43]

On the other hand, in the intermittent contact regime, where CNT's are more often used for imaging purposes, the possibility of CNT slipping or pinning may add hurdles to accurate topographical studies but also supply opportunities for surface composition mapping. For example, CNT2 and CNT3 were used to image a sample of OG sheets on HOPG, as shown in Fig. 7, with setpoint amplitudes that ensured the CNTs were intermittently tapping the sample [see Figs. 5(b) and 5(c)]. From previous work,[52] the OG sheets are expected to be 0.67-nm thick, depending on the number of folds, while exhibiting a slightly lower phase lag due to differences in compositional chemistry. In Fig. 7(b), the phase images taken with CNT3 clearly contrast the OG sheet with the underlying HOPG while the topography difference is approximately equal to the thickness of a single OG sheet. The 8° phase difference is similar to results with conventional AFM probes (not shown).

When CNT2 was used to image the HOPG-OG sample in Fig. 7(a), the phase contrast between the samples was nearly 55°. This phase contrast, nearly an order of magnitude larger than that obtained with conventional probes, highlights the

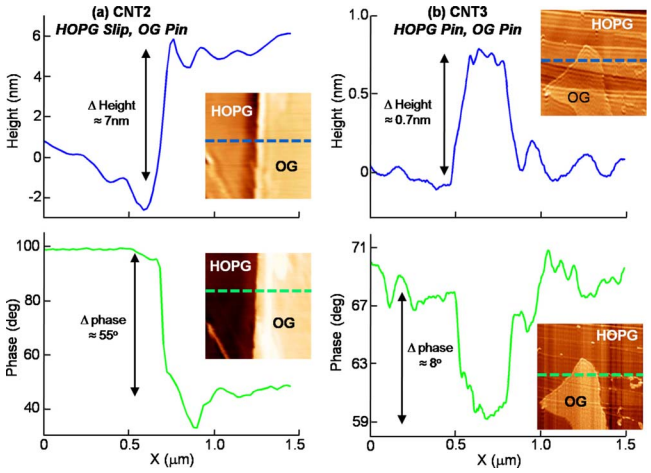


FIG. 7. (Color online) Topography and phase images with corresponding line scans produced with WSXM (Ref. 66) for CNT2 and CNT3 on an OG-HOPG sample. Whereas the OG-HOPG phase and height contrast produced with CNT3 (b) is similar to that of a conventional AFM probe, CNT2 (a) shows an enhanced phase contrast and topographical artifact because it tends to slip on HOPG while staying pinned on OG when intermittently tapping the substrate.

advantage of using CNT AFM probes with slipping boundary conditions for enhanced phase contrast imaging.[67] Because the enhanced phase contrast in this example is caused by CNT slip, certain CNT AFM probes, namely, ones with large angles from horizontal,[68,69] could prove useful for mapping the friction, surface roughness, and adhesion on different samples. However, this improved material contrast comes with the cost of degraded lateral resolution.

For example, CNT slipping may lead to unwanted topographical artifacts that must be carefully considered. In Fig. 7(a), the height change was $\approx 7$ nm, an unrealistical number that implies a stacking of 9+OG sheets. This topographical error can be explained with amplitude-distance curves of CNT2 in Fig. 5(b). For the chosen setpoint of 65 nm, there is $\Delta z \approx 6$ nm difference between the HOPG and OG amplitude curves, which is likely caused by the CNTs ability to slide easily on HOPG. This $\Delta z$ error manifests itself in the apparent $\approx 7$ nm height difference between OG-HOPG in Fig. 7(a), an artifact due to CNT sliding rather than sample topography.[33]

## VIII. CONCLUSIONS

In this work, we have demonstrated how to identify several oscillation regimes (attractive, intermittent contact with pinned or sliding boundary conditions, permanent point contact, and permanent line contact) for CNT AFM probes operated in AM-dAFM while systematically investigating whether CNT tips may either pin or slip on the surface depending on the type of material and the lateral forces that are present. Continuum CNT models with van der Waals interactions capable of large deformations were used with either a perfect slip or perfect pin boundary conditions to better explain static-force-distance measurements. Qualitative comparisons between experiments and theory suggested that CNTs could either initially pin or slip, depending on the surface. The type of CNT boundary condition was further investigated through dAFM analysis of intermittent contact. CNT slipping was particularly evident when tip-sample dissipation curves were plotted, highlighting the nonconservative interactions present when slipping. A clear understanding of the different oscillation regimes may provide new opportunities for improved biochemical applications, nanolithography, and CNT nanodevices while CNT slipping can potentially lead to topographical errors, improved phase contrast, and novel friction-mapping AFM modes.

## ACKNOWLEDGMENTS

This work was funded, in part, by the Purdue University graduate school. We are grateful to Deepak Pandey and Ron Reifenberger of Purdue University for providing the HOPG-OG samples integral to this work.

*Corresponding author; raman@purdue.edu

[1] H. Dai, J. H. Hafner, A. G. Rinzler, D. T. Colbert, and R. E. Smalley, Nature (London) **384**, 147 (1996).
[2] I. Fenoglio, M. Tomatic, D. Lison, J. Muller, A. Fonseca, J. B. Nagy, and B. Fubini, Free Radic Biol. Med. **40**, 1227 (2006).
[3] E. D. de Asis, Jr., Y. Li, R. Ohta, A. Austin, J. Leung, and C. V. Nguyen, Appl. Phys. Lett. **93**, 023129 (2008).
[4] G. Nagy, M. Levy, R. Scarmozzino, R. M. Osgood, Jr., H. Dai, R. E. Smalley, C. A. Michaels, G. W. Flynn, and G. F. McLane, Appl. Phys. Lett. **73**, 529 (1998).
[5] S. S. Wong, A. T. Woolley, T. W. Odom, J.-L. Huang, P. Kim, D. V. Vezenov, and C. M. Lieber, Appl. Phys. Lett. **73**, 3465 (1998).
[6] C. V. Nguyen, K.-J. Chao, R. M. D. Stevens, A. Cassel, J. Han, and M. Meyyappan, Nanotechnology **12**, 363 (2001).
[7] S. Rozhok, S. Jung, V. Chandrasekhar, X. Lin, and V. P. Dravid, J. Vac. Sci. Technol. B **21**, 323 (2003).
[8] T. Larsen, K. Moloni, F. Flack, M. A. Eriksson, M. G. Lagally, and C. T. Black, Appl. Phys. Lett. **80**, 1996 (2002).
[9] T. Ikuno, M. Katayam, M. Kishida, K. Kamada, Y. Murata, T. Yasuda, S. Honda, J.-G. Lee, H. Mori, and K. Oura, Jpn. J. Appl. Phys., Part 2 **43**, L644 (2004).
[10] W. Mizutani, N. Choi, T. Uchihashi, and H. Tokumoto, Jpn. J. Appl. Phys., Part 1 **40**, 4328 (2001).
[11] Z. Deng, E. Yenilmez, J. Leu, J. E. Hoffman, E. W. J. Straver, H. Dai, and K. A. Moler, Appl. Phys. Lett. **85**, 6263 (2004).
[12] H. Kuramochi, T. Uzumaki, M. Yasutake, A. Tanaka, H. Akinaga, and H. Yokoyama, Nanotechnology **16**, 24 (2005).
[13] M. Luna, P. J. de Pablo, J. Colchero, J. Gomez-Herrero, A. M. Baro, H. Tokumoto, and S. P. Jarvis, Ultramicroscopy **96**, 83 (2003).
[14] A. J. Austin, C. V. Nguyen, and Q. Ngo, J. Appl. Phys. **99**,

114304 (2006).
[15] M. Zhao, V. Sharma, H. Wei, R. R. Birge, J. A. Stuart, F. Papadimitrakopoulos, and B. D. Huey, Nanotechnology **19**, 235704 (2008).
[16] S. Takahashi, T. Kishida, S. Akita, and Y. Nakayama, Jpn. J. Appl. Phys., Part 1 **40**, 4314 (2001).
[17] H. Dai and N. Franklin, Appl. Phys. Lett. **73**, 1508 (1998).
[18] H. Kuramochi, T. Tokizaki, H. Yokoyama, and J. A. Dagata, Nanotechnology **18**, 135703 (2007).
[19] H. Kuramochi, T. Tokizaki, K. Ando, H. Yokoyama, and J. A. Dagata, Nanotechnology **18**, 135704 (2007).
[20] L. Chen, C. L. Cheung, P. D. Ashby, and C. M. Lieber, Nano Lett. **4**, 1725 (2004).
[21] J. H. Hafner, C.-L. Cheung, A. T. Wooley, and C. M. Lieber, Prog. Biophys. Mol. Biol. **77**, 73 (2001).
[22] H. Azehara, Y. Kasanuma, K. Ide, K. Hidaka, and H. Tokumoto, Jpn. J. Appl. Phys., Part 1 **47**, 3594 (2008).
[23] N. A. Kouklin, W. E. Kim, A. D. Lazareck, and J. M. Xu, Appl. Phys. Lett. **87**, 173901 (2005).
[24] M. J. Esplandiu, V. G. Bittner, K. P. Giapis, and C. P. Collier, Nano Lett. **4**, 1873 (2004).
[25] I. U. Vakarelski, S. C. Brown, K. Higashitani, and B. M. Moudgil, Langmuir **23**, 108903 (2007).
[26] S. P. Jarvis, T. Uchihashi, T. Ishida, and H. Tokumoto, J. Phys. Chem. B **104**, 6091 (2000).
[27] M. Kageshima, H. Jensenius, M. Dienwiebel, Y. Nakayama, H. Tokumoto, S. P. Jarvis, and T. H. Oosterkamp, Appl. Surf. Sci. **188**, 440 (2002).
[28] R. M. Stevens, C. V. Nguyen, and M. Meyyappan, IEEE Trans. Nanobiosci. **3**, 56 (2004).
[29] V. Barwich, M. Bammerlina, A. Baratoff, R. Bennewitz, M. Guggisberg, C. Loppacher, O. Pfeiffer, E. Meyer, H.-J. Güntherodt, J.-P. Salvetat, J.-M. Bonard, and L. Forró, Appl. Surf. Sci. **157**, 269 (2000).
[30] S. D. Solares, M. J. Esplandiu, W. A. Goddard II, and C. P. Collier, J. Phys. Chem. B **109**, 11493 (2005).
[31] S. I. Lee, S. W. Howell, A. Raman, R. Reifenberger, C. V. Nguyen, and M. Meyyappan, Ultramicroscopy **103**, 95 (2005).
[32] A. Kutana, K. P. Giapis, J. Y. Chen, and C. P. Collier, Nano Lett. **6**, 1669 (2006).
[33] D. Dietzel, S. Marsaudon, J. P. Aimé, C. V. Nguyen, and G. Couturier, Phys. Rev. B **72**, 035445 (2005).
[34] C. Bernard, S. Marsaudon, R. Boisgard, and J. P. Aimé, Nanotechnology **19**, 035709 (2008).
[35] D. Dietzel, M. Faucher, A. Iia, J. P. Aimé, S. Marsaudon, A. M. Bonnot, V. Bouchiat, and G. Couturier, Nanotechnology **16**, S73 (2005).
[36] S. Marsaudon, C. Bernard, D. Dietzel, C. V. Nguyen, A.-M. Bonnot, J.-P. Aimé, and R. Boisgard, in *Applied Scanning Probe Methods VIII*, edited by B. Bhusan, H. Fuchs, and M. Tomitori (Springer, US, New York, 2008).
[37] A. E. H. Love, *A Treatise on the Mathematical Theory of Elasticity* (Dover, New York, 1944).
[38] L. A. Girifalco, M. Hodak, and R. S. Lee, Phys. Rev. B **62**, 13104 (2000).
[39] M. C. Strus, L. Zalamea, A. Raman, R. B. Pipes, C. V. Nguyen, and E. A. Stach, Nano Lett. **8**, 544 (2008).
[40] M. C. Strus, R. R. Lahihi, P. Ares, V. López, A. Raman, and R. Reifenberger, Nanotechnology **20**, 385709 (2009).
[41] V. V. Dobrokhotov, M. M. Yazdanpanah, S. Pabba, A. Safir, and R. W. Cohn, Nanotechnology **19**, 035502 (2008).
[42] M. R. Falvo, G. J. Clary, R. M. Taylor II, V. Chi, F. P. Brooks, Jr., S. Washburn, and R. Superfine, Nature (London) **389**, 582 (1997).
[43] M. C. Strus, C. Cano, R. B. Pipes, C. V. Nguyen, and A. Raman, Compos. Sci. Technol. **69**, 1580 (2009).
[44] N. Sasaki, A. Toyoda, N. Itamura, and K. Miura, e-J. Surf. Sci. Nanotechnol. **6**, 72 (2008).
[45] M. Ishikawa, R. Harada, N. Sasaki, and K. Miura, Appl. Phys. Lett. **93**, 083122 (2008).
[46] X. Oyharcabal and T. Frisch, Phys. Rev. E **71**, 036611 (2005).
[47] D. W. Coffin, L. A. Carlsson, and R. B. Pipes, Compos. Sci. Technol. **66**, 1132 (2006).
[48] K. Lee, B. Luki, A. Magrez, J. W. Seo, G. A. D. Briggs, A. J. Kulik, and L. Forr, Nano Lett. **7**, 1598 (2007).
[49] J. E. Sader and J. W. M. Chon, Rev. Sci. Instrum. **70**, 3967 (1999).
[50] E. J. Doedel, H. B. Keller, and J. P. Kernévez, Int. J. Bifurcation Chaos Appl. Sci. Eng. **1**, 493 (1991).
[51] R. M. D. Stevens, N. A. Frederick, B. L. Smith, D. E. Morse, G. D. Stucky, and P. K. Hansma, Nanotechnology **11**, 1 (2000).
[52] D. Pandey, R. Reifenberger, and R. Piner, Surf. Sci. **602**, 1607 (2008).
[53] S. I. Lee, S. W. Howell, A. Raman, R. Reifenberger, C. V. Nguyen, and M. Meyyappan, Nanotechnology **15**, 416 (2004).
[54] H. W. Yap, R. S. Lakes, and R. W. Carpick, Nano Lett. **7**, 1149 (2007).
[55] B. Bhushan, X. Ling, A. Jungen, and C. Hierold, Phys. Rev. B **77**, 165428 (2008).
[56] M. C. Strus, A. Raman, C.-S. Han, and C. V. Nguyen, Nanotechnology **16**, 2482 (2005).
[57] A. N. Jiang, S. Gao, X. L. Wei, X. L. Liang, and Q. Chen, J. Phys. Chem. C **112**, 15631 (2008).
[58] S. Akita, H. Nishikima, and Y. Nakayama, J. Phys. D: Appl. Phys. **33**, 2673 (2000).
[59] Q. Ye, A. M. Cassell, H. Liu, K.-J. Chao, J. Han, and M. Meyyappan, Nano Lett. **4**, 1301 (2004).
[60] B. Anczykowski, B. Gotmann, H. Fuchs, and J. P. Cleveland, Appl. Surf. Sci. **140**, 376 (1999).
[61] R. Garcia, C. J. Gòmez, N. F. Martinez, C. Dietz, and R. Magerle, Phys. Rev. Lett. **97**, 016103 (2006).
[62] M. Ishikawa, M. Yoshimura, and K. Ueda, Appl. Surf. Sci. **188**, 456 (2002).
[63] S. Hu and A. Raman, Appl. Phys. Lett. **91**, 123106 (2007).
[64] W.-P. Huang, H.-H. Cheng, S.-R. Jian, D.-S. Chuu, J.-Yn. Hsieh, C.-M. Lin, and M.-S. Chiang, Nanotechnology **17**, 3838 (2006).
[65] J. S. Choi, S. Bae, S. J. Ahn, D. H. Kim, K. Y. Jung, C. Han, C. C. Chung, and H. Lee, Ultramicroscopy **107**, 1091 (2007).
[66] I. Horcas, R. Fernández, J. M. Gómez-Rodríguez, J. Colchero, J. Gómez-Herrero, and A. M. Baro, Rev. Sci. Instrum. **78**, 013705 (2007).
[67] Z. W. Xu, Y. C. Liang, S. Dong, Y. Z. Cao, T. Q. Zhao, J. H. Wang, and Q. L. Zhao, Ultramicroscopy **105**, 72 (2005).
[68] S. D. Solares, Y. Matsuda, and W. A. Goddard III, J. Phys. Chem. B **109**, 16658 (2005).
[69] R. Schlaf, Y. Emirov, J. A. Bieber, A. Sikder, J. Kohlscheen, D. A. Walters, M. R. Isla, B. Metha, Z. F. Ren, T. L. Shofner, B. B. Rossie, and M. W. Cresswell, Proc. SPIE **4689**, 53 (2002).